Molecular dynamics simulation of fibronectin adsorption on peptoid brushes

David L. Cheung*,† and King Hang Aaron Lau*,‡

†*School of Biological and Chemical Science, University of Galway, Galway, Ireland*

‡*Department of Pure and Applied Chemistry, University of Strathclyde, Glasgow, UK*

E-mail: david.cheung@universityofgalway.ie; aaron.lau@strathclyde.ac.uk

Abstract

In recent years there has been significant interest in the development of material surfaces that can control their interactions with proteins for mediating subsequent cell attachment. Such biointerfaces can have applications in e.g. medical devices and biosensors. However, non-specific adsorption of unrelated proteins and other biomolecules present in the cell environment can potentially mask the intended protein presentation. Recently surface-grafted peptoid-based polymer brushes, both neutral and zwitterionic, have emerged as candidate surfaces for resisting protein adsorption and anti-fouling applications due to their strong hydration and chain flexibility. On the other hand, specific peptoid sequences may also be prepared to enable specific protein binding interactions. However, molecular level insight into peptoid and brush interactions with proteins are both lacking. Using atomistic molecular dynamics simulation, we investigated the interaction of the fibronectin (Fn) FnIII_{9-10} domains, which exhibit fibronectin's integrin cell adhesive motifs, with neutral polysarcosine and a sequence specific zwitterionic analog. As expected, peptoids simulated at different grafting densities exhibited protein adsorbing and antifouling regimes. however, comparison of independent adsorption simulations, including with different starting

orientations of the protein, identified regions of $FnIII_{9-10}$ that are typically involved in peptoid interactions, suggesting a degree of specificity in this. The binding regions were distinct from the integrin binding motifs and different interactions were observed between polysarcosine and the zwitterionic sequence. Unlike typical protein-surface adsorption, the specific interactions are driven by polar interactions. These observations give new insight into protein-surface interactions, which can be used to guide the development of new biomaterials.

Introduction

Surfaces that can control the adsorption of proteins are important in many applications.[1,2] Adsorption of proteins onto medical implants can lead to unfavourable immune and inflammatory responses, so controlling this is important in the creation of materials for biomedical applications.[3] Protein adsorption is also a key step in the attachment of organisms onto surfaces,[4] so understanding and controlling this vital in preventing biofilm formation in medical settings[5] and on attachment of molluscs to marine surfaces.[6] Interactions between proteins and surfaces also effects cell growth and can be used to control the cell differentiation, for the creation of living biomaterials.[7,8] Due to this there has been much interest in developing materials that can control protein adsorption, with a wide-range of surfaces investigated.[9] This work has generated some general rules for the development of anti-fouling materials, such as high wettibility, presence hydrogen-bond acceptors, and lack of hydrogen bond donors, although exceptions to these exist.[10] Zwitterionic polymers have attracted particular interest as anti-fouling materials;[11] these are typically hydrophilic (so are highly wettable) and the presence of both positive and negative charges can lead to a complex electrostatic environment.[12] However, due to the interplay between factors such as surface hydration, electrostatic potential, and steric effects, understanding the origin of anti-fouling behaviour for these materials is challenging.

While many different types of material have been investigated for biomaterials, sur-

faces consisting of peptoid chains grafted onto them to form a polymer brush have been shown to be particular attractive.[13–17] Peptoids (*N*-substituted glycines) are peptidomimetic molecules,[18,19] with the side chains being attached to amine nitrogen rather than the alpha carbon. This shift in side chain position affects the chain flexibility (through the removal of the backbone hydrogen bonding). Peptoids can be synthesised using similar solid-phase techniques as peptides,[20] allowing for the creation of chains with precise lengths and sequences, which makes them an ideal experimental system for the investigation of polymer sequence design. A number of studies have been performed on peptoid brushes, showing that these can be grafted onto surfaces to form polymer brushes. These brushes can resist the adsorption of proteins and bacteria, making them promising candidates for biomaterial surfaces. To optimise the design of peptoid sequences for these applications and to give insight into factors that determine protein behaviour it is important to understand the structures of these surfaces and the molecular interactions between them and proteins.

Understanding the interaction between proteins and surfaces requires knowledge of interactions and processes on the molecular level. This can be performed using a range of experimental methods. Reflectivity and scattering experiments using neutrons or X-rays can give insight into the brush and protein structure, as can surface sensitive spectroscopy techniques such sum frequency generation spectroscopy. Ellipsometry or quartz crystal microbalance with dissipation monitoring can be used to determine the amount of protein adsorbed. The strength of protein-surface interaction can be estimated using atomic force microscopy or surface force apparatus measurements.

To complement experiment, computational studies using molecular dynamics (MD) simulations can also be used to investigate of protein-surface interactions.[21] These give direct access to the molecular level, so can give microscopic detail that is challenging to determine experimentally. Over the past two decades protein adsorption onto surfaces has been investigated in a many studies using MD simulation. These have given significant insight into the molecular factors that control protein adsorption, such as the role of surface bound

water, surface structure,[22,23] and surface chemistry.[24] While these have often focused on simple surfaces, including inorganic surfaces, such as metals[25] or silica,[26] and self-assembled monolayers,[27] increasingly these have started to target more complex surfaces, such as polymers[28,29] (crystalline or amorphous) and brushes.[30] Simulations of these, even in the absence of proteins, have identified features,[31,32] such as surface hydration and mobility, that are correlated with protein resistance. Explicit simulation of the interaction of these more complex surfaces with proteins is necessary to more fully understand these factors.

In this paper we build on this previous work by using molecular dynamics simulations to investigate the adsorption and interaction of a fibronectin fragment onto peptoid brushes. Fibronectin is found in high concentrations in blood and plays important roles in cell adhesion and inflammatory response,[33] so the interaction between fibronectin and material surfaces is important in determining the body's response to implanted medical devices. It is also the target for a number of bacteria[34] so adsorption of fibronectin onto device surfaces can also be an initial step in implant-associated infections. Surfaces have been shown to drive the formation of fibronectin fibrils that can be used on the control of cell differentiation[35] and the binding of growth factors.[36] The particular fragment that is investigated consisted of the ninth and tenth type-III domains (FnIII_{9-10}). These contain the biologically important synergy (PHRSN) and cell-binding (RGD) motifs, so play a key role in the function of the protein. Two different brushes, either neutral brushes composed of polysarcosine or zwitterionic brushes (using peptoid analogs of lysine and glutamic acid for the cationic and anionic residues), were studied, with surface grafting densities below and above the critical values needed for protein resistance (full details of the simulations are given in the following section).

Model and Methodology

Following previous work the peptiod brush[32] was constructed from a placing a regular array of fully extended peptoid molecules on a rutile surface (with the C-terminal DOPA anchoring group close to the surface). To this was added a single protein, consisting of the $FnIII_{9-10}$ domains, in the bulk liquid above the surface (Figure 1(a)). Brushes containing two different peptoid sequences were studied; PS20 and PSKE20 (Figure 1(b)). The former is the neutral 20-mer polysarcosine composed of Na, the simplest peptoid and analog of alanine. (Following a recent proposal,[37,38] names of residues peptoid start with "N" for the sidechain substitution at the backbone nitrogen, followed by the 1-letter code of the amino acid for direct analogs of natural residues). Polysarcosine is a well-known antifouling peptoid and potential replacement of polyethylene glycol (PEG). PSKE20 is the (pseudo-)zwitterionic charge-balanced analog of PS20, with specific cationic Nk (analog of K—lysine) and anionic Ne substitutions (analog of E—glutamic acid), which we have previously studied.[16,32] Both peptoid chains had a terminal anchoring group (DOPA-Lys-DOPA-Lys-DOPA), linked to the surface. The rutile (110) surface was 16 and 34 unit cells in the x and y directions, giving a size of 104.9 Å and 101.2 Å and the slab had a thickness of 16 Å in the z-direction. For each brush two grafting densities 0.11 nm^{-2} and 0.56 nm^{-2} (corresponding to 12 and 60 chains respectively, i.e. Nchain=12 and Nchain=60) were considered. These grafting densities are, respectively, below and above the critical grafting density (~ 0.50 nm^{-2}) needed to suppress protein adsorption in for both brushes.[16] To fix the peptoid chains to the surface the z-coordinate of the Hζ atoms of the terminal DOPA residues were constrained to 1.78 Å above the highest oxygen atom in the rutile surface (corresponding to the minimum in the LJ potential between these atoms). As the constraint was only applied to the z-coordinate the peptoid chains retained mobility in the plane of the surface. Prior to the insertion of the protein, these surfaces were solvated and chloride counter-ions added to neutralise the system. Each surface was then energy minimized and a 100 ns molecular dynamics simulation was performed to generate an initial structure for the brush.

The initial structure of the protein was taken from the protein database (1FNF[39]), with the $FnIII_9$ and $FnIII_{10}$ domains corresponding to residues 1-89 and 90-184 respectively. This was placed above the brush surface, with its centre-of-mass ∼8 nm from the rutile surface; this made the lowest atom-atom separation between the protein and the brush at least 2 nm. To try to sample over different protein orientations nine simulations were performed for each surface. Three different orientations of the protein long axis in the x-y plane were considered (along x, along y, and at 45 degrees to the x-axis) and for each of these three different orientations of the synergy (PHRSN) and cell recognition (RGD) motifs (pointing away from surface, towards surface, and parallel to surface) were used. Note as experimental work considered adsorption of the full fibronectin protein rather than isolated domains,[27] conformations where the termini of these domains were oriented towards the surface were not considered.

Table 1: Definition of starting proteins orientations for each simulation. See Figure 1 for illustration of initial positions of cell-binding and synergy motifs.

Run	PHRSN/RGD orientation	Long axis orientation
1	Away from surface	Along x
2	Toward from surface	Along x
3	Parallel to surface	Along x
4	Away from surface	Along y
5	Toward from surface	Along y
6	Parallel to surface	Along y
7	Away from surface	45 degrees to x
8	Toward from surface	45 degrees to x
9	Parallel to surface	45 degrees to x

The charmm27 force field,[40] extended to consider peptoids[41] and non-natural amino acids,[42] was used for the protein and brush along with the charmm-TIP3P[43] water model were used. The rutile surface was modelled using the potential of Predota *et al.*[44]

Van der Waals interactions were evaluated with a cut off of 12 Å, with corrections to the energy and pressure applied. Electrostatic interactions were evaluated using a particle-mesh Ewald sum[45] with a real space cut off of 12 Å and a reciprocal space grid of 48×48×280.

All simulations were performed using the Gromacs molecular dynamics package (version 2018.4).[46–48] The system was energy minimised using the steepest descents algorithm, followed by short (10 ps) NVT simulations. Simulations were performed at 298 K, with temperature controlled using the velocity rescaling algorithm[49] with a relaxation time of 0.1 ps. For each system simulations of 200 ns were performed (with a timestep of 2 fs), with coordinates saved every 10 ps, giving a total simulation time of 7.2 μs across all systems. Bonds involving hydrogen atoms were constrained using the LINCS[50] algorithm and the geometry of water molecules was held rigid using the SETTLE algorithm.

Analysis of the simulations was performed using standard gromacs utilities and in-house python scripts using the MDAnalysis library.[51] Hydrogen bonds were identified using a donar-acceptor cutoff of 3 Å and donar-hydrogen-acceptor angle greater than 150°. Simulation snapshots were generated using VMD[52] (visual molecular dynamics).

To estimate the adsorption free energy (ΔG_{ads}) molecular mechanics Poission-Boltzmann surface area (MM-PBSA) calculations[53] were used. ΔG_{ads} was calculated according to

$$\Delta G_{ads} = G_{protein-surf} - G_{protein} - G_{surf} \tag{1}$$

where $G_{protein-surf}$ is the free energy of the protein-surface system and $G_{protein}$ and G_{surf} were the free energies of the protein and surface on their own. The calculations were performed using the single trajectory approach, where the free energies were calculated from a single simulation of the system. The free energy for each system was given by the sum of the molecular mechanics (E_{MM}) and solvation (G_{solv}) energies

$$G = E_{MM} + G_{solv} = E_{MM} + G_{PB} + G_{SA}. \tag{2}$$

where the solvation energy consists of polar solvation (G_{PB}) and non-polar solvation (G_{SA}) contributions. The conformation entropy is neglected due to the inaccuracy associated with its calculation and the limited influence this has on the calculated values.[54] The molecular

mechanics energy was given by

$$E_{MM} = E_{int} + E_{vdw} + E_{elec} \tag{3}$$

where the terms are the internal (bonded), VDW, and electrostatic energies. Note that for the single trajectory method the internal energy of the protein-surface complex is the same as the internal energies of the protein and surface added together, so this does not contribute to the value of the adsorption free energy. The non-polar solvation energy was calculated according to[55]

$$G_{SA} = \gamma SASA \tag{4}$$

where $SASA$ is the solvent accessible surface area, $\gamma = 0.005$ kcal mol^{-1} Å^{-2} was the surface tension. A probe radius of 1.4 Å was used in the calculation of $SASA$. The polar solvation energy was calculated using a Poisson-Boltzmann solver, with internal and external dielectric constants of 1 and 80. The MM-PBSA calculations were performed using the MMPBSA.py script,[56] part of the Amber package (version 18).

Results

Trajectories of Fibronectin Interaction

Figure 2 shows the evolution of the FnIII$_{9-10}$centre-of-mass positions over the 36 different trajectories simulated (200 ns each). As expected, for both PS20 and PSKE20 grafted at the lower Nchain=12 density (i.e., 0.11 nm^{-2}), the protein was seen to drop dramatically towards the underlying titania (Figures 2(a) and (c)). This process indicated penetration of the protein into peptoid layer and took up to roughly 125 ns for PS20 and a shorter 100 ns for PSKE20. Since the grafting density was below the critical density of ca. 0.5 nm^{-2},[16] this can be understood to represent protein adsorption, when there is an insufficient density of polymer chains to form an antifouling brush.

For Nchain=60 (i.e., 0.56 nm^{-2}; Fig. 2(b) and (d)), above the critical density, $FnIII_{9-10}$ remained above the peptoid layers throughout all trajectories. Nonetheless, like the case at lower Nchain=12 density, the protein positions trended downwards and this process also took a shorter time for PSKE vs. PS (roughly <50 ns vs. up to 75 ns, respectively). Unlike the case at lower chain density, there is no correlation in the interaction energy with distance to the surface (see 'Energetics and intermolecular interactions' below), and there is a clear "floor" of the protein position indicating that the peptoid brushes were able to prevent penetration to the underlying titania. This floor was at a higher height for PSKE20 than for PS20 (ca. 70∼80 Å vs. 65∼75 Å), reflecting the higher chain compression of the higher-molecular weight zwitterionic peptoid. (See later discussion for snapshots of the protein-peptoid interactions.) In all cases, the relatively shorter times taken for PSKE20 and the protein to come into to contact suggest that the zwitterionic sequence may have a different and stronger attractive interaction with fibronectin. This was unexpected given the generally favourable antifouling properties of zwitterionic brushes.

Modes of interaction

It was further observed that there may be different peptoid interaction modes distinguished by which of the domains, $FnIII_9$ or $FnIII_{10}$ came closer to the surface. As specified in Table 1, each simulation for a peptoid type and grafting density started with the protein placed in a different orientation with respect to the peptoid surface. However, comparison of the average centre-of-mass of each domain (Figure 3) shows that the peptoid-protein interactions may be classified as either 9-down (average $FnIII_9$ z-position is lower than that of $FnIII_{10}$ by more than the sum of their standard deviations), 10-down ($FnIII_{10}$ domain is lower), or even (difference less than the sum of standard deviations) (see Table 2 for summary). Although all the different modes can be observed for all surfaces, 10-down is more common for PS20, and both modes are roughly equally likely for PSKE20. The comparatively more favorable interaction of the 10-domain for PS20 may be due to a match between the less hydrophilic

nature of $FnIII_{10}$ (average hydrophobicity value of -0.454 vs. -0.115 for the net -1e charge $FnIII_{10}$) and the lower polarity of the neutral PS20 vs. the zwitterionic PSKE20, and vice versa.

Table 2: Number of simulations with $FnIII_9$ down, $FnIII_{10}$ down, or even.

Surface	9-down	10-down	even
PS20, Nchain=12	2	4	3
PS20, Nchain=60	2	4	3
PS20 (total)	4	8	6
PSKE20, Nchain=12	2	3	4
PSKE20, Nchain=60	3	3	3
PSKE20 (total)	5	6	7

We further investigated whether specific sequences may be closer to the surface than average and hence may be associated with peptoid interactions (Figure 4(a)). For the $FnIII_9$ domain, the I23-I29 and N76-G86 segments were found to be typically involved in adsorption, while A102-L109 and T148-G151 of $FnIII_{10}$ are closer to the surface (see Table 3 for sequences; G1-G7 between the 9 and 10 domains was also typically close to the surface but this is the inter-domain linker and is unlikely to be relevant for adsorption of the full protein). Notably, however, the functionally important synergy (PHRSN) and cell binding (RGD) motifs are not found close to the surface (Figure 4(b)).

Since the aforementioned interaction segments contain a number of polar and charged residues, electrostatic and dipole interactions may be the main contributions to the attractive interactions (see further discussion in section C). This also corroborates the consideration of overall domain polarity in driving the aforementioned 9-down and 10-down modes of interactions. Moreover, some of the interacting segments overlap with past studies. Simulations of $FnIII_{8-10}$ adsorption found that the T104-T106 region of the 10-domain was associated with adsorption onto a polar (OH-terminated) self-assembled monolayers (SAM).[57] In another study, T106 and G151 (as well as N132 and G136) were also found to be involved in FnIII9-10 adsorption onto an OH-terminated SAM.[58]

Table 3: Key protein regions and residues for protein interaction with peptoid brushes.

Domain	Region	Residues
$FnIII_9$	I23-I29	IAPRATI
	N76-G86	NGREESPLLIG
$FnIII_{10}$	A102-L109	AATPTSLL
	T148-G151	TISG

The interacting segments were further verified in analyses of individual trajectories. Figure 5(a) shows the residue z-coordinates for representative examples of 10-down adsorption (specifically corresponding to run 5 for PS20, Nchain=12, run 1 PS20, Nchain=60, run 9 PSKE20, Nchain=12, and run 3 PSKE20, Nchain=60). These trajectories were typified by consistently low z-coordinates for the same residues in the 10-domain as the simulations progressed, indicating long-lasting contacts formed with the peptoid surfaces. Note these correspond to different starting orientations of the protein suggesting that the simulations are long enough to allow for reorientation away from this and are unbiased in this respect.

To compare the interactions of the different peptoid surfaces we can examine the average difference between the z-coordinate of each residue and the protein centre-of-mass (Figure 5(b)). This is calculated over the last 50 ns of each simulation, where the protein had achieved stable positions relative to the brush. For all but the low chain density PS20 Nchain=12 brush, the trends were similar, with the two PSKE20 example surfaces shown almost identical. This suggests a degree of specificity on the binding onto the brush, with both the A102-L109 and T148-G151 segments found close to the surface. For the Nchain=12 PS20 brush, only the A102-L109 region in the 10-domain is found near the peptoid surface and the adjacent $FnIII_9$ domain was pulled closer to the brush (Figure 5(c)). It appears that penetration of the $FnIII_{10}$ domain into the brush and its adsorbed orientation is responsible for bringing the $FnIII_9$ domain close enough to adsorb onto the surface. For the other surfaces the orientation of $FnIII_{10}$ on the brush allows the $FnIII_9$ domain to remain in solution.

For the 9-down interactions (Figure 6) we see more commonality in the adsorbed protein

configuration between the different surfaces (exemplar cases shown are runs 6 and 4 for PS20 at Nchain=12 and 60, respectively, and run 7's for PSKE20 at Nchain=12 and 60, respectively), indicating a stronger specific association of this domain. While Figure 6(a) shows the long-lasting contacts of the FnIII9 interaction segments described earlier, as well as an additional E128-N132 region found close to the surface for PS20 at Nchain=60, Figure 6(b) most clearly shows the commonality in the residue positions across protein interactions with the different brushes. Interestingly, $FnIII_9$ interactions were also observed to be associated with a degree of $FnIII_{10}$ interaction. These are seen as lighter but also long-lasting contacts (Figure 6(a)) of the $FnIII_{10}$ interaction segments in the trajectories (i.e., A102-L109 and T148-G151) that either coincided with or started after the $FnIII_9$ interaction segments (i.e., I23-I29 and N76-G86) becoming associated with the surface. Since these interacting regions are at the ends of the $FnIII_9$ and $FnIII_{10}$ domains, the tandem protein structure has to adopt a more bent conformation and lie "flat" on the brush, which is quite different from the 10-down case where the protein remains more linear with the $FnIII_9$ domain typically projecting above the brush into the solution.

Energetics and intermolecular interactions

To understand the driving forces for fibronectin association with the peptoids, the free energies of protein interaction/adsorption with the different peptoid brushes were calculated. Moreover, the numbers of hydrogen bonds as well as the interacting residues on both the protein and the brush were analyzed.

MM-PBSA calculations showed that, as expected, the total interaction was more attractive for the denser Nchain=60 surfaces with more peptoid chains (Figure 7). For example, for the neutral PS20, the median energy decreased from -37 kcal mol^{-1} for Nchain=12 to -70 kcal mol^{-1} for Nchain=60 The interaction is also higher for the corresponding charge balanced PSKE20 brushes (median energies of -50 kcal mol^{-1} and -80 kcal mol^{-1} for Nchain=12 and 60, respectively). This corroborates earlier observations of, e.g., the shorter simulation times

needed for the fibronectin domain positions to trend towards the peptoid layers. However, the increases in the magnitude of interaction energies going to the denser brush is much less than the factor of five difference in chain densities between the Nchain=12 and 60 surfaces, which reflects our earlier observation that the Nchain=60 brushes retained an antifouling effect (i.e., $FnIII_{9-10}$ does not penetrate the denser brush).

As the interaction energy should depend on the protein distance from the surface in the case of adsorption, it is useful to examine the correlation between the average protein position and interaction free energies across the different simulation runs for each system (Figure 8). For the low density Nchain=12 surfaces a larger, more negative energy is indeed noticeably trending with the protein being at a lower surface height as it penetrated into the peptoid layer, indicating adsorption on the peptoid-rutile surface. For denser Nchain=60 brushes there is no such correlation. This decoupling between interaction energy and height position suggests that the attraction of $FnIII_{9-10}$ towards the peptoids simulated represents a different phenomenon, e.g., reversible adsorption.

Shown in Figure 9 are the average numbers of hydrogen bonds formed between the protein and peptoid brush in each simulation. For PS20, the number of hydrogen bonds formed were similar for both grafted chain densities (2.85 bonds at Nchain = 12 and 3.29 bonds at Nchain = 60). For PSKE20, significantly more hydrogen bonds were formed, with 6.32 and 12.20 bonds at Nchain = 12 and 60, respectively. While charged residues typically form more hydrogen bonds, this effect may be especially enhanced since we previously found that the bulkier Nk and Ne charged residues in PSKE20 are preferentially concentrated on the surface of the brush to reduce steric hindrance and the electrostatic potential.[32]

While many different protein residues on the protein exterior are involved in hydrogen bonding with the peptoids, some residues were found in a number of the simulations (Table 4). Generally these were polar or charged residues and, as may be expected, only a few hydrophobic residues (L83, I85) were found to participate in hydrogen bonding. For the neutral PS20 brush, most of the protein residues involved were correspondingly neu-

tral polar ones. For the zwitterionic PSKE20 brush, charged protein residues were more commonly involved, especially when interacting with the lower density PSKE20 Nchain=12 layer that $FnIII_{9-10}$ was able to penetrate. This likely reflected the simultaneous electrostatic attractions with oppositely signed residues in the peptoid.

Table 4: Residues forming hydrogen bonds with peptoid brush in multiple simulations. Number in parentheses give number of simulation runs where that protein residue forms a hydrogen bond with the peptoid brush.

	Protein residues
PS20, Nchain=12	T6 (2), A24 (2), R78 (2), L83 (3), Q87 (2), E99 (4), T148 (2)
PS20, Nchain=60	G1 (2), T6 (2), A24 (2), R26 (4), T104 (3), R120 (2), Y121 (2), T139 (2), K144 (5), T148 (4), R183 (2)
PSKE20, Nchain=12	D9 (5), R26 (5), T28 (2), R35 (2), E39 (3), E67 (4), R78 (5), Q87 (3), D97 (2),E99 (5), D113 (3), R120 (3), E128 (2), K144 (3), Y182 (2), R183 (3)
PSKE20, Nchain=60	G1 (4), T6 (2), D9 (7), D12 (2), R26 (6), T28 (2), E39 (3), S42 (2), N55 (3), E67 (4), R78 (6), I85 (2), E80 (5), Q87 (3), Q88 (2), E99 (5), T104 (2), S107 (2), W112 (2), D113 (5), T118 (2), R120 (4), S143 (2), K144 (7), S145 (3), T146 (2), T148 (2), S150 (2), D157 (2), R183 (3)

Turning to the average number of hydrogen bonds with peptoid residues, Figure 10 shows bonding differences corresponding to brush densities and peptoid types that further detail and corroborate the protein-peptoid interactions. In parallel to Figure 9, significantly fewer number of hydrogen bonds were seen with the PS20 chains. Meanwhile, the majority of the increased number of hydrogen bonds with PSKE chains were associated with the charged Nk and Ne residues (Figure 10). In fact, the number of bonds with the neutral Na were relatively fewer when Nk and Ne were present (compare, e.g., Figure 10 (b) and (d)). Moreover, the number of hydrogen bonds with Ne were typically higher than with Nk, possibly reflecting Ne's higher polarity (i.e., Ne's ethylene vs. Nk's butylene linker, and two nucleophilic oxygen atoms in Ne's acid group vs. Nk's single amine). In addition, only for the sparser brushes (Figure 10(a) and (c)), hydrogen bonds were also seen to form with the Lys and DOPA residues anchoring the peptoid chains to bottom titania surface, confirming

protein penetration into the interior of the brush.

Fibronectin Mobility on Peptoid Brushes

A central feature of fibronectin is its multimerization/assembly into fibrils, for which diffusion on the surface is needed. Comparison between the in-plane motion of $FnIII_{9-10}$ on the different surfaces (Figure 11(a)) suggests that the protein is more mobile among the Nchain=12 chains, reflecting the greater volume of voids within the peptoid layer at Nchain=12. On the densier Nchain=60 brushes, our results show that the protein remains at the top of these peptoid brushes, the lower mobility within the simulated time-scale seen may reflect the attractive interactions between fibronectin and the peptoids. This higher mobility on the sparser brushes may promote fibril formation on these compared to denser surfaces.

The in-plane diffusion coefficient (D_{xy}) was also calculated to quantify the mobility (Figure 11(b)). Corroborating the in-plane motion shown visually (Figure 11(a)), the highest mobilities were obtained for the sparser Nchain = 12 layers. A wider variation in D_{xy} and higher mobilities were also seen for the neutral PS20 compared to the zwitterionic PSKE20 at a corresponding chain density, which might lead to differences in fibronectin fibril formation.

Conclusions

Using atomistic MD simulation, the interaction of $FnIII_{9-10}$ with peptoid brushes was investigated in detail. The peptoids studied were a neutral PS20 polysarcosine and a zwitterionic PSKE20 analog. While the present MD results are consistent with previous experimental observations indicating that both peptoids could resist gross protein adsorption, they also reveal that fibronectin interacts with peptoids via certain specific interactions, especially when the peptoids are grafted on the surface below their critical chain density and proteins can penetrate in between the peptoid chains. Moreover, by performing simulations from different initial protein orientations, two general modes of adsorption were identified. In

"10-down" interactions, $FnIII_{10}$ is preferentially oriented towards the peptoid surface based on polar interactions of the A102-L109 and T148-G151 fragments. In "9-down" interactions, $FnIII_9$ is first brought closer to the surface, with association of the even more hydrophilic and/or charged I23-I29 and N76-G86 regions, which then bring $FnIII_{10}$ to co-adsorb. Both modes are equally likely for PSKE20, but there appears to be a preference for 10-down for PS20.

In our system, notably the biologically relevant synergy (PHRSN) and cell binding (RGD) motifs are not involved in the peptoid interactions. Moreover, the interactions are driven by a combination of polar and electrostatic interactions as well as hydrogen bonding, and are distinct from the hydrophobic interactions that commonly drive non-specific protein adsorption. Additionally, MM-PBSA free energy calculations and other lines of evidence indicate a stronger attraction of fibronectin to PSKE20 that is driven by hydrogen bonding with Ne and Nk charged residues.

Hydrophilic peptoids such as PS20 and PSKE20 are conventionally promoted as antifouling sequences. However, our MD analysis has revealed that specific fibronectin residues can drive specific polar interactions with the hydrophilic peptoids in 9-down and 10-down configurations. This may have relevance to phenomena such as the generation of different soft protein coronas even around nanoparticles functionalized by antifouling surfaces.[59,60] On the other hand, our results further showed that $FnIII_{9-10}$ adsorbed on low density peptoid layers can exhibit relatively high surface mobilities for promoting fibronectin multimerization into extracellular matrix fibrils. Since the fibronectin synergy (PHRSN) and cell binding (RGD) motifs are located, respectively, on the $FnIII_9$ and $FnIII_{10}$ domains, our results also hold out the intriguing possibility of enabling oriented and specific fibronectin surface presentations that can be evaluated in future cell culture experiments.

Acknowledgements

Computational resources were provided by the SFI/HEA funded Irish Centre for High End Computing. DC and KHAL thank the Royal Society of Edinburgh for Saltire International Collaboration research support (ref. 1979).

References

(1) Maan, A. M. C.; Hofman, A. H.; De Vos, W. M.; Kamperman, M. Recent Developments and Practical Feasibility of Polymer-Based Antifouling Coatings. *Advanced Functional Materials* **2020**, *30*, 2000936.

(2) Xu, X.; Chang, Y.; Gong, Y.; Zhang, Y.; Yu, Y.; Peng, H.; Fu, C. Recent Advances in Antifouling Surface Polymer Brushes. *ACS Applied Polymer Materials* **2024**, *6*, 1–27.

(3) Chen, Q.; Zhang, D.; Gu, J.; Zhang, H.; Wu, X.; Cao, C.; Zhang, X.; Liu, R. The Impact of Antifouling Layers in Fabricating Bioactive Surfaces. *Acta Biomaterialia* **2021**, *126*, 45–62.

(4) Cai, S.; Wu, C.; Yang, W.; Liang, W.; Yu, H.; Liu, L. Recent Advance in Surface Modification for Regulating Cell Adhesion and Behaviors. *Nanotechnology Reviews* **2020**, *9*, 971–989.

(5) Lisoń, J.; Taratuta, A.; Paszenda, Z.; Szindler, M.; Basiaga, M. Perspectives in Prevention of Biofilm for Medical Applications. *Coatings* **2022**, *12*, 197.

(6) Li, Y.; Cao, Y. The Molecular Mechanisms Underlying Mussel Adhesion. *Nanoscale Advances* **2019**, *1*, 4246–4257.

(7) Murphy, W. L.; McDevitt, T. C.; Engler, A. J. Materials as Stem Cell Regulators. *Nature Materials* **2014**, *13*, 547–557.

(8) Rodrigo-Navarro, A.; Sankaran, S.; Dalby, M. J.; Del Campo, A.; Salmeron-Sanchez, M. Engineered Living Biomaterials. *Nature Reviews Materials* **2021**, *6*, 1175–1190.

(9) Blaszykowski, C.; Sheikh, S.; Thompson, M. Surface chemistry to minimize fouling from blood-based fluids. *Chemical Society Reviews* **2012**, *41*, 5599.

(10) Rodriguez-Emmenegger, C.; Brynda, E.; Riedel, T.; Houska, M.; Šubr, V.; Alles, A. B.; Hasan, E.; Gautrot, J. E.; Huck, W. T. S. Polymer Brushes Showing Non-Fouling in Blood Plasma Challenge the Currently Accepted Design of Protein Resistant Surfaces. *Macromol. Rapid Commun.* **2011**, *32*, 952–957.

(11) Ci, J.; Kang, H.; Liu, C.; He, A.; Liu, R. Protein resistance adsorption mechanism and applications of zwitterionic polymers. *Progress in Chemistry* **2015**, *27*, 1198–1212.

(12) Chen, S.; Li, L.; Zhao, C.; Zheng, J. Surface hydration: Principles and applications toward low-fouling/nonfouling biomaterials. *Polymer* **2010**, *51*, 5283–5293.

(13) Lau, K. H. A.; Ren, C.; Sileika, T. S.; Park, S. H.; Szleifer, I.; Messersmith, P. B. Surface-grafted polysarcosine as a peptoid antifouling polymer brush. *Langmuir* **2012**, *28*, 16099–16107.

(14) Ham, H. O.; Park, S. H.; Kurutz, J. W.; Szleifer, I. G.; Messersmith, P. B. Antifouling glycocalyx-mimetic peptoids. *Journal of the American Chemical Society* **2013**, *135*, 13015–13022.

(15) Lau, K. H. A. Peptoids for biomaterials science. *Biomaterials Science* **2014**, *2*, 627.

(16) Lau, K. H. A.; Sileika, T. S.; Park, S. H.; Sousa, A. M. L.; Burch, P.; Szleifer, I.; Messersmith, P. B. Molecular Design of Antifouling Polymer Brushes Using Sequence-Specific Peptoids. *Advanced Materials Interfaces* **2015**, *2*, 1400225/1–10.

(17) Gao, Q.; Li, P.; Zhao, H.; Chen, Y.-S.; Jiang, L.; Ma, P. X. Methacrylate-ended

Polypeptides and Polypeptoids for Antimicrobial and Antifouling Coatings. *Polymer Ch* **2017**, *8*, 6386–6397.

(18) Simon, R. J.; Kania, R. S.; Zuckermann, R. N.; Huebner, V. D.; Jewell, D. A.; Banville, S.; Ng, S.; Wang, L.; Rosenberg, S.; Marlowe, C. K. Peptoids: a modular approach to drug discovery. *Proc. Natl. Acad. Sci. U.S.A.* **1992**, *89*, 9367–9371.

(19) Zuckermann, R. N. Peptoid origins. *Biopolymers* **2011**, *96*, 545–555.

(20) Sun, J.; Zuckermann, R. N. Peptoid Polymers: A Highly Designable Bioinspired Material. *ACS Nano* **2013**, *7*, 4715–4732.

(21) Ozboyaci, M.; Kokh, D. B.; Corni, S.; Wade, R. C. Modeling and simulation of protein-surface interactions: Achievements and challenges. *Quarterly Reviews of Biophysics* **2016**, *49*, 1–45.

(22) Penna, M.; Ley, K.; Maclaughlin, S.; Yarovsky, I. Surface heterogeneity: a friend or foe of protein adsorption – insights from theoretical simulations. *Faraday Discuss.* **2016**, *191*, 435–464.

(23) Cheung, D. L. Effect of surface chemistry on islet amyloid polypeptide conformation. *Biointerphases* **2020**, *15*, 051001.

(24) Kubiak-Ossowska, K.; Mulheran, P. A.; Nowak, W. Fibronectin Module FNIII9 Adsorption at Contrasting Solid Model Surfaces Studied by Atomistic Molecular Dynamics. *Journal of Physical Chemistry B* **2014**, *118*, 9900–9908.

(25) Brancolini, G.; Corazza, A.; Vuano, M.; Fogolari, F.; Mimmi, M. C.; Bellotti, V.; Stoppini, M.; Corni, S.; Esposito, G. Probing the Influence of Citrate-Capped Gold Nanoparticles on an Amyloidogenic Protein. *ACS Nano* **2015**, *9*, 2600–2613.

(26) Kubiak-Ossowska, K.; Tokarczyk, K.; Jachimska, B.; Mulheran, P. A. Bovine Serum

Albumin Adsorption at a Silica Surface Explored by Simulation and Experiment. *The Journal of Physical Chemistry B* **2017**, *121*, 3975–3986.

(27) Bieniek, M. K.; Llopis-Hernandez, V.; Douglas, K.; Salmeron-Sanchez, M.; Lorenz, C. D. Minor Chemistry Changes Alter Surface Hydration to Control Fibronectin Adsorption and Assembly into Nanofibrils. *Advanced Theory and Simulations* **2019**, *2*, 1900169.

(28) O' Brien, C. P.; Stuart, S. J.; Bruce, D. A.; Latour, R. A. Modeling of Peptide Adsorption Interactions with a Poly (Lactic Acid) Surface. *Langmuir* **2008**, *24*, 14115–14124.

(29) Mallinson, D.; Cheung, D. L.; Simionesie, D.; Mullen, A. B.; Zhang, Z. J.; Lamprou, D. A. Experimental and computational examination of anastellin (FnIII1c)-polymer interactions. *Journal of Biomedical Materials Research - Part A* **2017**, *105*, 737–745.

(30) Song, X.; Man, J.; Qiu, Y.; Wang, J.; Li, R.; Zhang, Y.; Cui, G.; Li, J.; Li, J.; Chen, Y. Study of Hydration Repulsion of Zwitterionic Polymer Brushes Resistant to Protein Adhesion through Molecular Simulations. *ACS Applied Materials & Interfaces* **2024**, *16*, 17145–17162.

(31) Sheikh, S.; Blaszykowski, C.; Nolan, R.; Thompson, D.; Thompson, M. On the hydration of subnanometric antifouling organosilane adlayers: A molecular dynamics simulation. *Journal of Colloid and Interface Science* **2015**, *437*, 197–204.

(32) Cheung, D. L.; Lau, K. H. A. Atomistic Study of Zwitterionic Peptoid Antifouling Brushes. *Langmuir* **2019**, *35*, 1483–1494.

(33) Dalton, C. J.; Lemmon, C. A. Fibronectin: Molecular Structure, Fibrillar Structure and Mechanochemical Signaling. *Cells* **2021**, *10*, 2443.

(34) Vaca, D. J.; Thibau, A.; Schütz, M.; Kraiczy, P.; Happonen, L.; Malmström, J.; Kempf, V. A. J. Interaction with the Host: The Role of Fibronectin and Extracellular Matrix Proteins in the Adhesion of Gram-negative Bacteria. *Medical Microbiology and Immunology* **2020**, *209*, 277–299.

(35) Salmerón-Sánchez, M.; Rico, P.; Moratal, D.; Lee, T. T.; Schwarzbauer, J. E.; García, A. J. Role of Material-Driven Fibronectin Fibrillogenesis in Cell Differentiation. *Biomaterials* **2011**, *32*, 2099–2105.

(36) Llopis-Hernández, V.; Cantini, M.; González-García, C.; Cheng, Z. A.; Yang, J.; Tsimbouri, P. M.; García, A. J.; Dalby, M. J.; Salmerón-Sánchez, M. Material-Driven Fibronectin Assembly for High-Efficiency Presentation of Growth Factors. *Science Advances* **2016**, *2*, e1600188.

(37) Swanson, H. W. A.; Lau, K. H. A.; Tuttle, T. Minimal Peptoid Dynamics Inform Self-Assembly Propensity. *The Journal of Physical Chemistry B* **2023**, *127*, 10601–10614.

(38) Swanson, H. W. A.; Lau, K. H. A.; Tuttle, T. *A Convention for Peptoid Monomer Naming*; 2023.

(39) Leahy, D. J.; Aukhil, I.; Erickson, H. P. 2.0 Å Crystal Structure of a Four-Domain Segment of Human Fibronectin Encompassing the RGD Loop and Synergy Region. *Cell* **1996**, *84*, 155–164.

(40) MacKerell, A. D. et al. All-Atom Empirical Potential for Molecular Modeling and Dynamics Studies of Proteins †. *The Journal of Physical Chemistry B* **1998**, *102*, 3586–3616.

(41) Mirijanian, D. T.; Mannige, R. V.; Zuckermann, R. N.; Whitelam, S. Development and use of an atomistic CHARMM-based forcefield for peptoid simulation. *Journal of Computational Chemistry* **2014**, *35*, 360–370.

(42) Gfeller, D.; Michielin, O.; Zoete, V. SwissSidechain: A molecular and structural database of non-natural sidechains. *Nucleic Acids Research* **2013**, *41*, 327–332.

(43) Mark, P.; Nilsson, L. Structure and dynamics of the TIP3P, SPC, and SPC/E water models at 298 K. *Journal of Physical Chemistry A* **2001**, *105*, 9954–9960.

(44) Predota, M.; Bandura, a. V.; Cummings, P. T.; Kubicki, J. D.; Wesolowski, D. J.; Chialvo, a. a.; Machesky, M. L.; Pr, M. Electric Double Layer at the Rutile (110) Surface . 1 . Structure of Surfaces and Interfacial Water from Molecular Dynamics by Use of ab Initio Potentials Electric Double Layer at the Rutile (110) Surface . 1 . Structure of Surfaces and Interfacial Wa. *Journal of Physical Chemistry B* **2004**, *108*, 12049–12060.

(45) Essmann, U.; Perera, L.; Berkowitz, M. L.; Darden, T.; Lee, H.; Pedersen, L. G. A smooth particle mesh Ewald method. *Journal of Chemical Physics* **1995**, *103*, 8577.

(46) Van Der Spoel, D.; Lindahl, E.; Hess, B.; Groenhof, G.; Mark, A. E.; Berendsen, H. J. C. GROMACS: Fast, flexible, and free. *Journal of Computational Chemistry* **2005**, *26*, 1701–1718.

(47) Hess, B.; Kutzner, C.; van der Spoel, D.; Lindahl, E. GROMACS 4: Algorithms for Highly Efficient, Load-Balanced, and Scalable Molecular Simulation. *J. Chem. Theory Comput.* **2008**, *4*, 435–447.

(48) Abraham, M. J.; Murtola, T.; Schulz, R.; Páll, S.; Smith, J. C.; Hess, B.; Lindahl, E. GROMACS: High performance molecular simulations through multi-level parallelism from laptops to supercomputers. *SoftwareX* **2015**, *1-2*, 19–25.

(49) Bussi, G.; Donadio, D.; Parrinello, M. Canonical sampling through velocity rescaling. *Journal of Chemical Physics* **2007**, *126*, 014101/1–7.

(50) Hess, B.; Bekker, H.; Berendsen, H. J. C.; Fraaije, J. G. E. M. LINCS: A linear constraint solver for molecular simulations. *Journal of computational chemistry* **1997**, *18*, 1463–1472.

(51) Michaud-Agrawal, N.; Denning, E. J.; Woolf, T. B.; Beckstein, O. MDAnalysis: A Toolkit for the Analysis of MolecularDynamics Simulations. *Journal of computational chemistry* **2011**, *32*, 2319–2327.

(52) Humphrey, W.; Dalke, A.; Schulten, K. VMD: Visual molecular dynamics. *Journal of Molecular Graphics* **1996**, *14*, 33–38.

(53) Srinivasan, J.; Cheatham, T. E.; Cieplak, P.; Kollman, P. A.; Case, D. A. Continuum Solvent Studies of the Stability of DNA, RNA, and Phosphoramidate-DNA Helices. *Journal of the American Chemical Society* **1998**, *120*, 9401–9409.

(54) Hou, T.; Wang, J.; Li, Y.; Wang, W. Assessing the Performance of the MM/PBSA and MM/GBSA Methods. 1. The Accuracy of Binding Free Energy Calculations Based on Molecular Dynamics Simulations. *Journal of Chemical Information and Modeling* **2011**, *51*, 69–82.

(55) Sitkoff, D.; Sharp, K. A.; Honig, B. Accurate Calculation of Hydration Free Energies Using Macroscopic Solvent Models. *The Journal of Physical Chemistry* **1994**, *98*, 1978–1988.

(56) Miller, B. R.; McGee, T. D.; Swails, J. M.; Homeyer, N.; Gohlke, H.; Roitberg, A. E. *MMPBSA.py* : An Efficient Program for End-State Free Energy Calculations. *Journal of Chemical Theory and Computation* **2012**, *8*, 3314–3321.

(57) Liamas, E.; Kubiak-Ossowska, K.; Black, R.; Thomas, O.; Zhang, Z.; Mulheran, P. Adsorption of Fibronectin Fragment on Surfaces Using Fully Atomistic Molecular Dynamics Simulations. *International Journal of Molecular Sciences* **2018**, *19*, 3321.

(58) Li, T.; Hao, L.; Li, J.; Du, C.; Wang, Y. Role of Ninth Type-III Domain of Fibronectin in the Mediation of Cell-Binding Domain Adsorption on Surfaces with Different Chemistries. *Langmuir* **2018**, *34*, 9847–9855.

(59) Lynch, I.; Cedervall, T.; Lundqvist, M.; Cabaleiro-Lago, C.; Linse, S.; Dawson, K. A. The Nanoparticle–Protein Complex as a Biological Entity; a Complex Fluids and Surface Science Challenge for the 21st Century. *Advances in Colloid and Interface Science* **2007**, *134–135*, 167–174.

(60) Lundqvist, M.; Stigler, J.; Elia, G.; Lynch, I.; Cedervall, T.; Dawson, K. A. Nanoparticle Size and Surface Properties Determine the Protein Corona with Possible Implications for Biological Impacts. *Proceedings of the National Academy of Sciences* **2008**, *105*, 14265–14270.

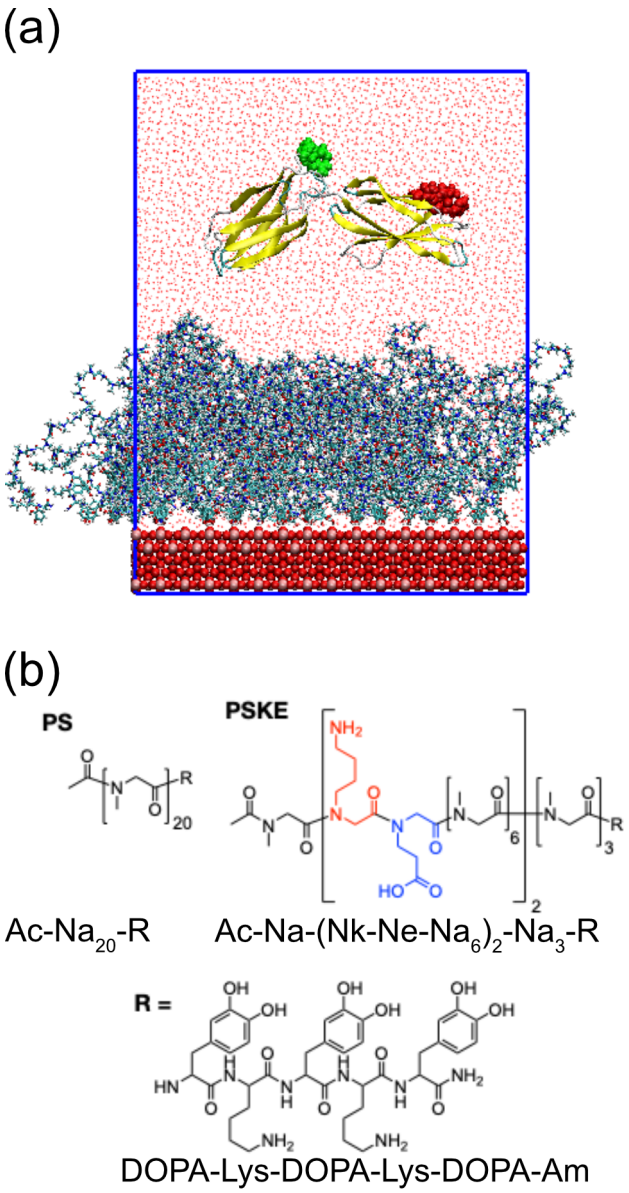

Figure 1: (a) Example of initial simulation structure. PHRSN (synergy) and RGD (cell recognition) motifs highlighted as red and green spheres respectively. (b) Chemical structures of the PS20 and PSKE20 peptoids simulated. The sequences are specified under each structure. Peptoid residue names, according to a recent proposal, start with "N" to indicate the backbone nitrogen sidechain substitution, followed by the 1-letter code of the amino acid).[37,38]

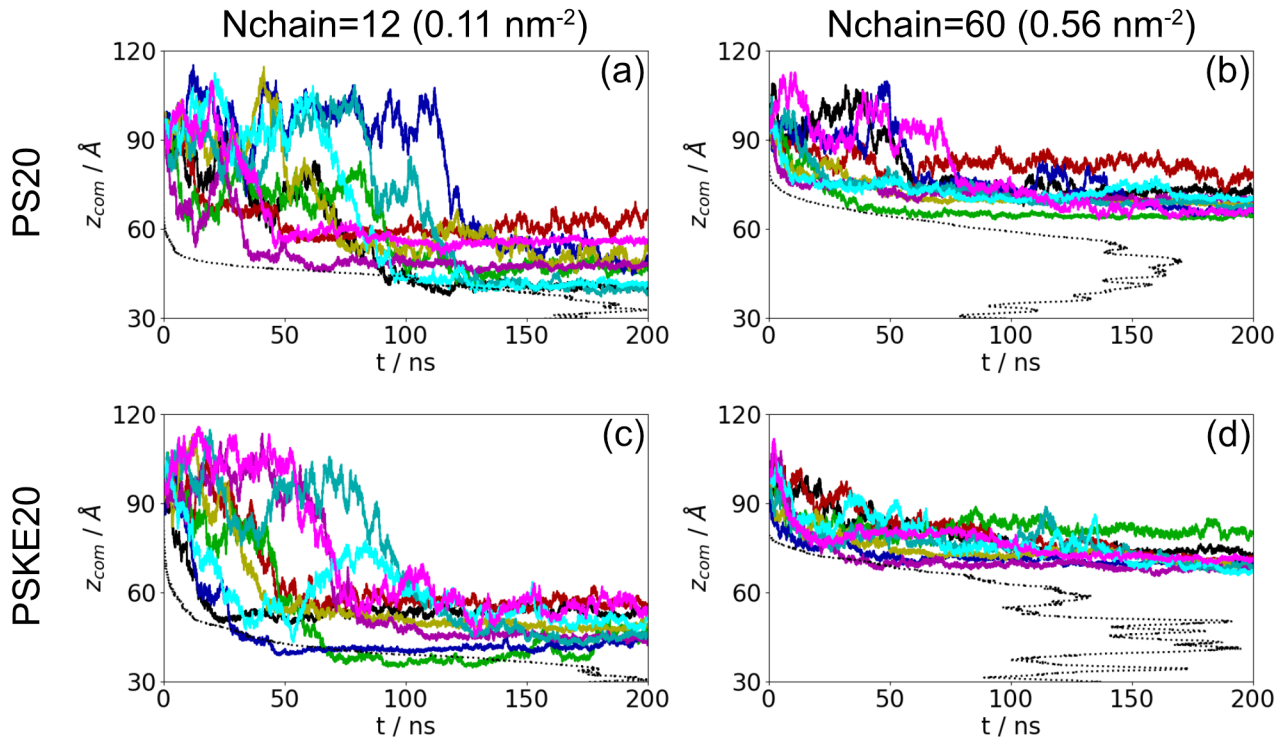

Figure 2: Protein centre-of-mass positions for $FnIII_{9-10}$ on PS20 Nchain=12 (top left), PS20 Nchain=60 (top right), PSKE20 Nchain=12 (bottom left), and PSKE20 Nchain=60 (bottom right). Black, red, green, blue, yellow, purple, turquoise, cyan, and magenta denote runs 1-9 respectively. Dotted black line shows brush density profile.

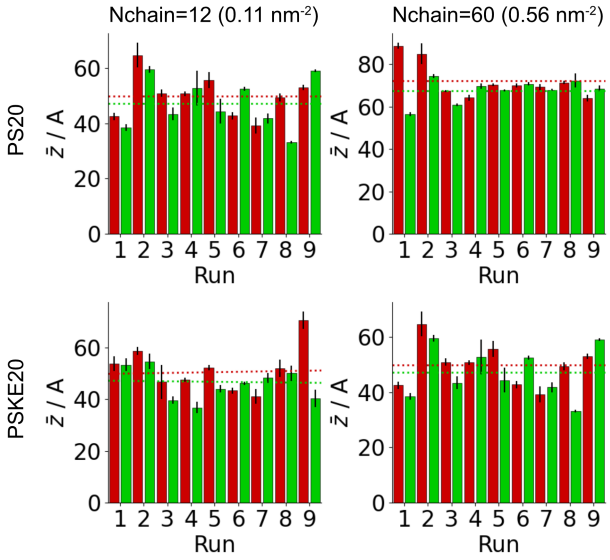

Figure 3: Average centre-of-mass positions for $FnIII_9$ and $FnIII_{10}$ domains from simulations of $FnIII_{9-10}$ on PS20 Nchain=12 (top left), PS20 Nchain=60 (top right), PSKE20 Nchain=12 (bottom left), and PSKE20 Nchain=60 (bottom right). Red and green show centre-of-mass positions for $FnIII_9$ and $FnIII_{10}$ domains respectively. Dotted lines show average values for each system.

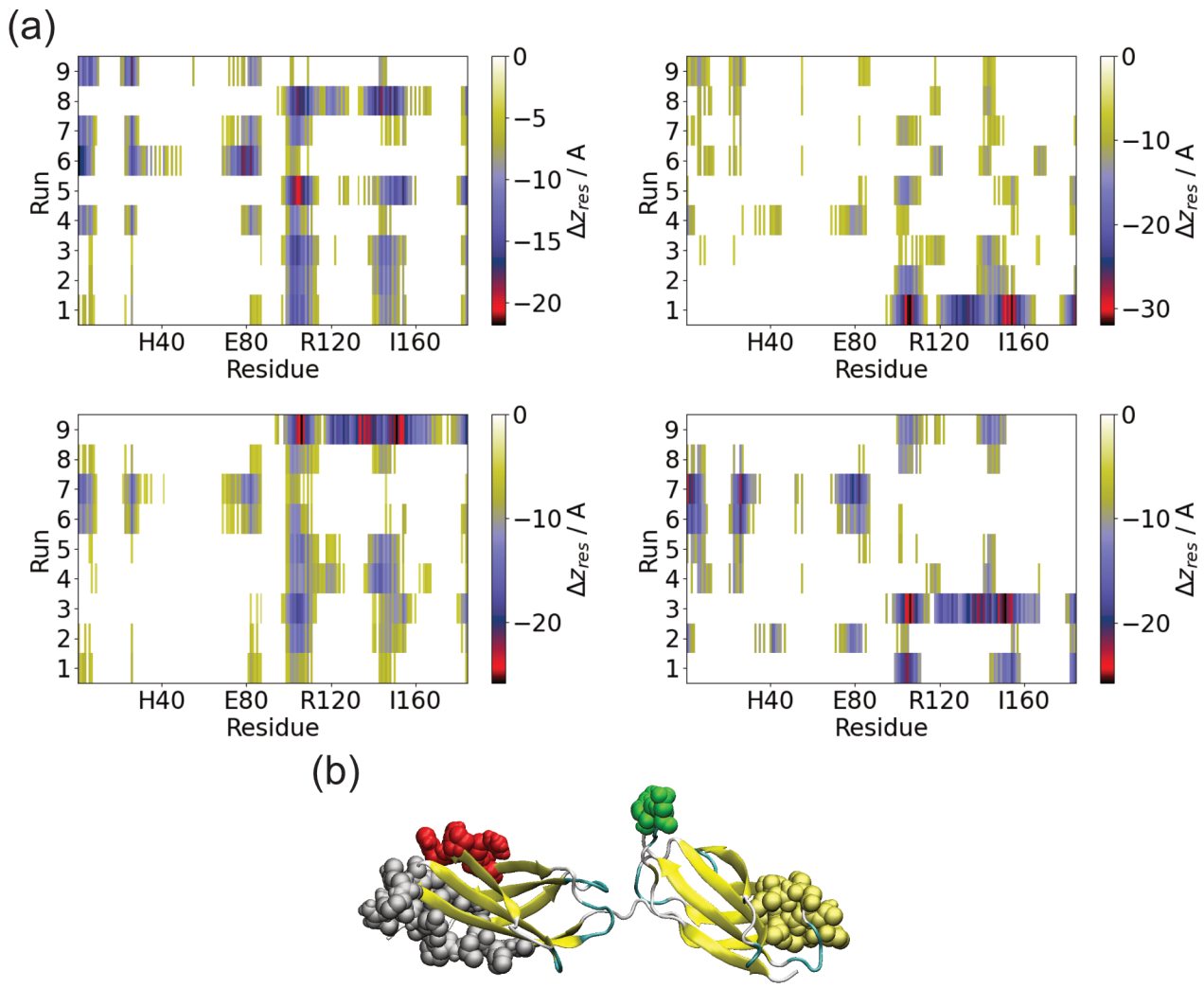

Figure 4: (a) Difference between average residue centre-of-mass and protein centre-of-mass positions for $FnIII_{9-10}$ on PS20 Nchain=12 (top left), PS20 Nchain=60 (top right), PSKE20 Nchain=12 (bottom left), and PSKE20 Nchain=60 (bottom right). (b) Structure of FnIII-9-10 with regions involved in adsorption highlighted (silver and gold show regions in $FnIII_9$ and $FnIII_{10}$ domains respectively). Synergy and cell binding motifs highlighted in red and green.

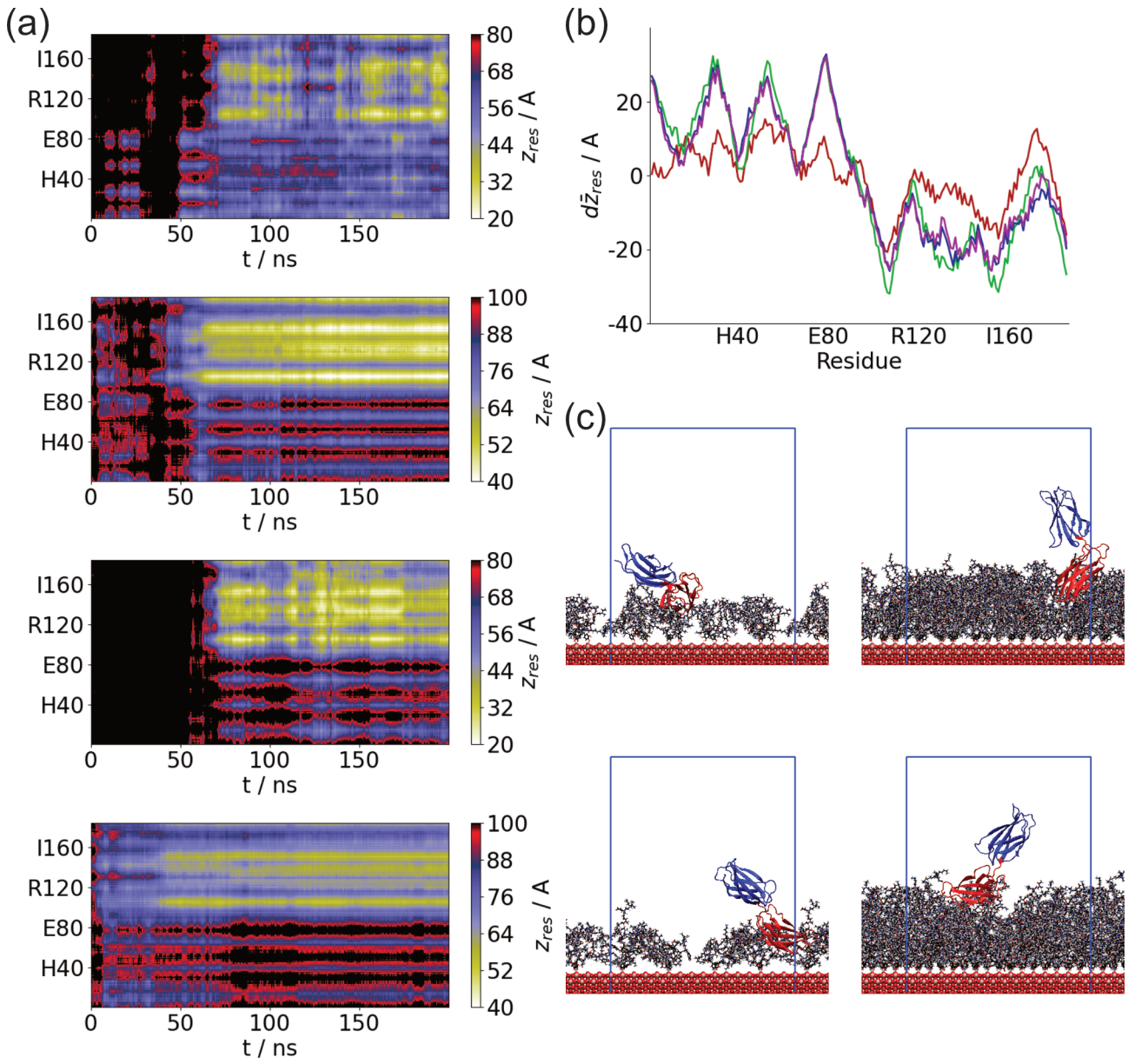

Figure 5: Adsorption for exemplar 10-down simulations (details in text). (a) Residue centre-of-mass z co-ordinates for (top to bottom) PS20, Nchain=12, PS20, Nchain=60, PSKE20, Nchain=12, and PSKE20,Nchain=60. (b) Average difference between residue centre-of-mass and protein centre-of-mass z-co-ordinates. Red, green, blue, and magenta denote PS20, Nchain=12, PS20, Nchain=60, PSKE20, Nchain=12, and PSKE20, Nchain=60 respectively. (c) Representative snapshots for PS20, Nchain=12 (top left) ,PS20, Nchain=60 (top right), PSKE20, Nchain=12 (bottom left), and PSKE20, Nchain=60 (bottom right).

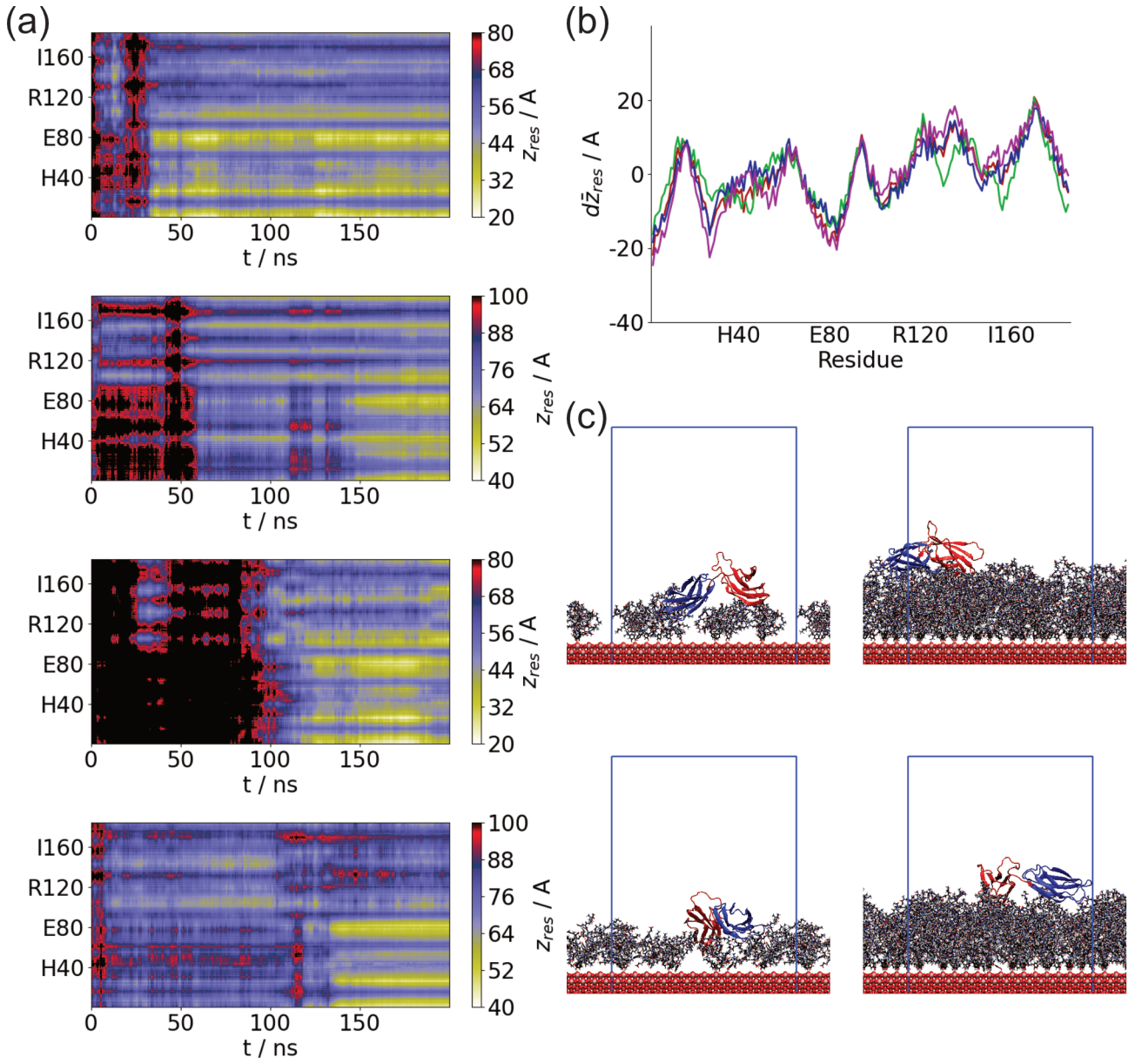

Figure 6: Adsorption for exemplar 9-down simulations (details in text). (a) Residue centre-of-mass z co-ordinates for (top to bottom) PS20, Nchain=12, PS20, Nchain=60, PSKE20, Nchain=12, and PSKE20, Nchain=60. (b) Average difference between residue centre-of-mass and protein centre-of-mass z-co-ordinates. Red, green, blue, and magenta denote PS20, Nchain=12,PS20, Nchain=60, PSKE20, Nchain=12, and PSKE20, Nchain=60 respectively. (c) Representative snapshots for PS20, Nchain=12 (top left), PS20, Nchain=60 (top right), PSKE20, Nchain=12 (bottom left), and PSKE20, Nchain=60 (bottom right).

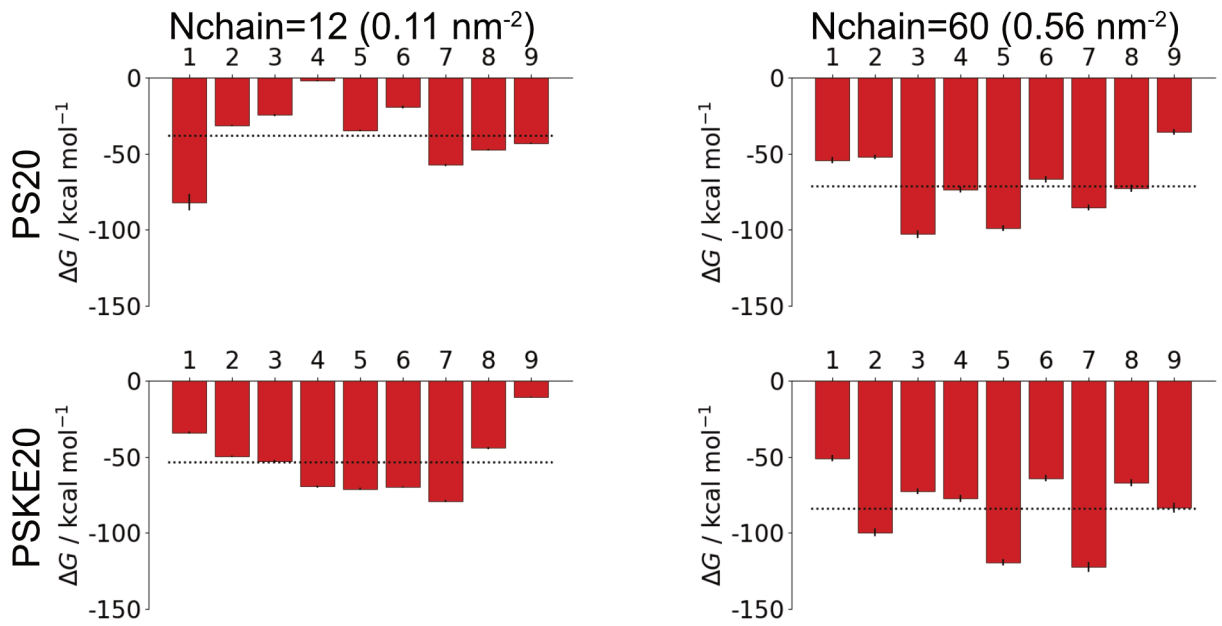

Figure 7: Average adsorption free energies for each simulation run for (top to bottom) $FnIII_{9-10}$ on PS20 Nchain=12, PS20 Nchain=60, PSKE20 Nchain=12, and PSKE20 Nchain=60. Dotted line shows average across all runs.

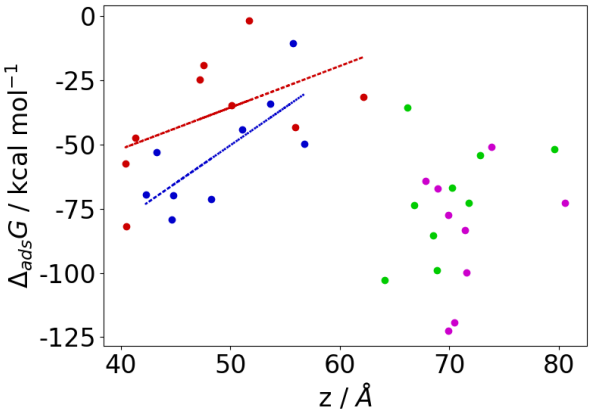

Figure 8: Correlation between average protein-surface interaction energy and protein centre-of-mass position. Red, green, blue, and magenta denote PS20, Nchain=12, PS20, Nchain=60, PSKE20, Nchain=12, and PSKE20, Nchain=60 respectively.

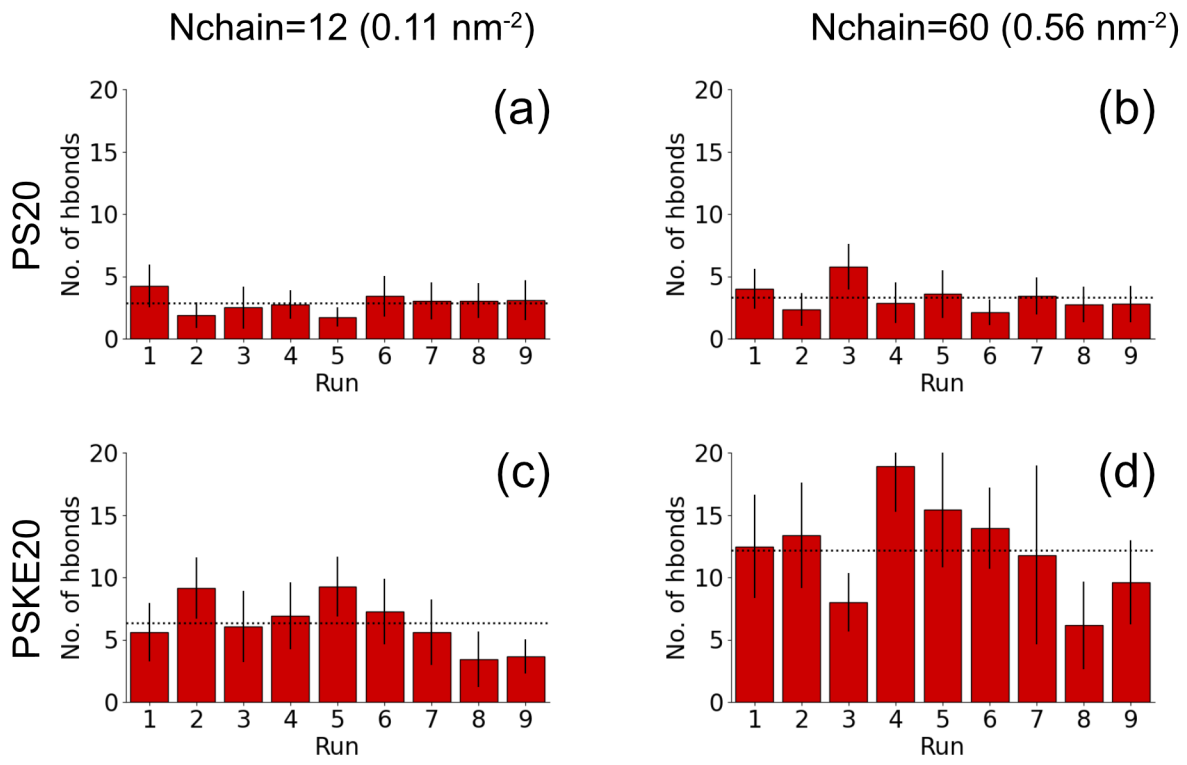

Figure 9: Average number of protein-peptoid hydrogen bonds for (a) PS20, Nchain=12, (b) PS20, Nchain=60, (c) PSKE20, Nchain=12, and (d) PSKE20, Nchain=60 (bottom right).

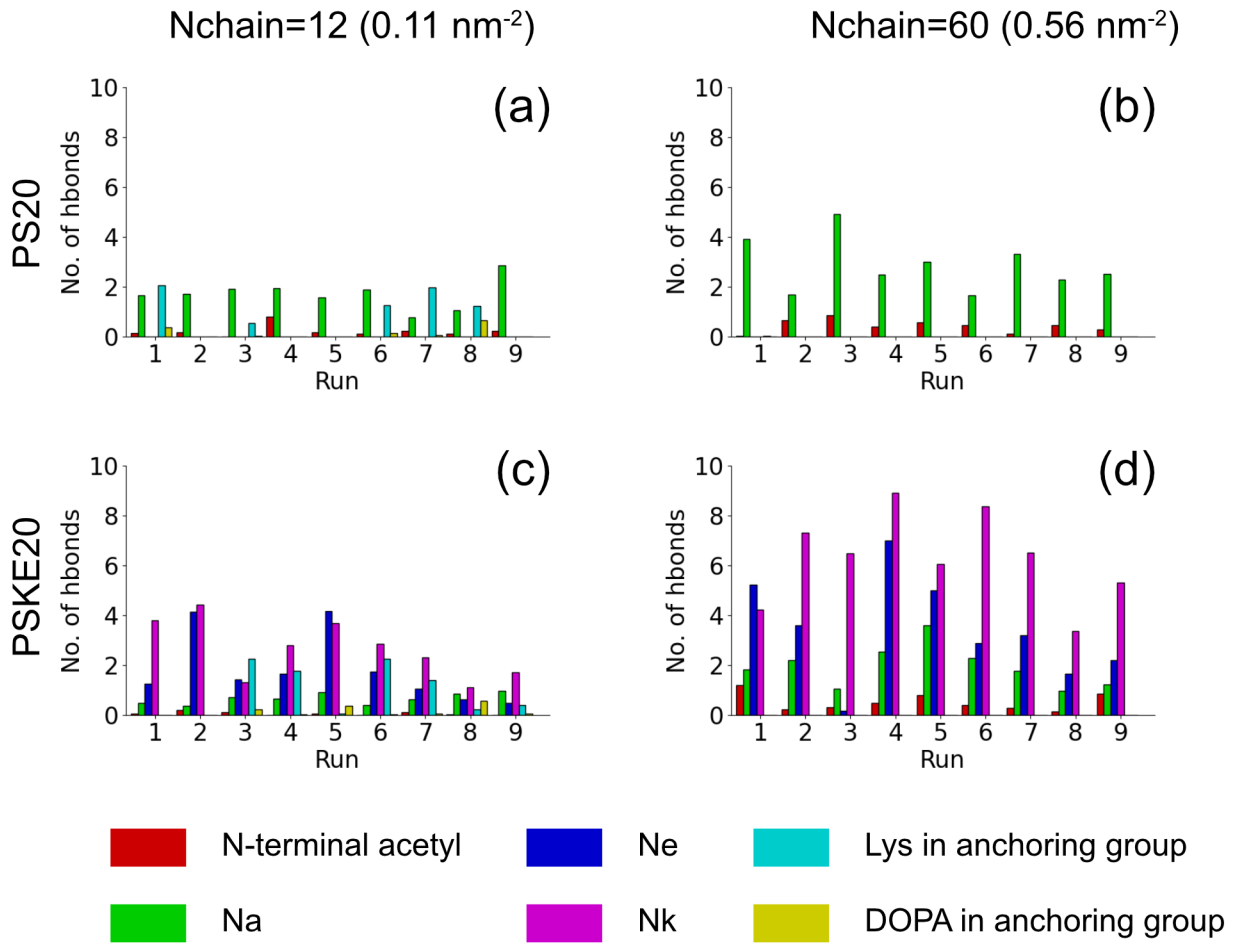

Figure 10: Average number of protein-peptoid hydrogen bonds formed for different types of peptoid residues for (a) PS20, Nchain=12, (b) PS20, Nchain=60, (c) PSKE20, Nchain=12, and (d) PSKE20, Nchain=60. Number of hydrogen bonds for Ace, Na, Nk, Ne, Arg, and DOPA residues denoted by red, green, blue, magenta, cyan, and gold respectively.

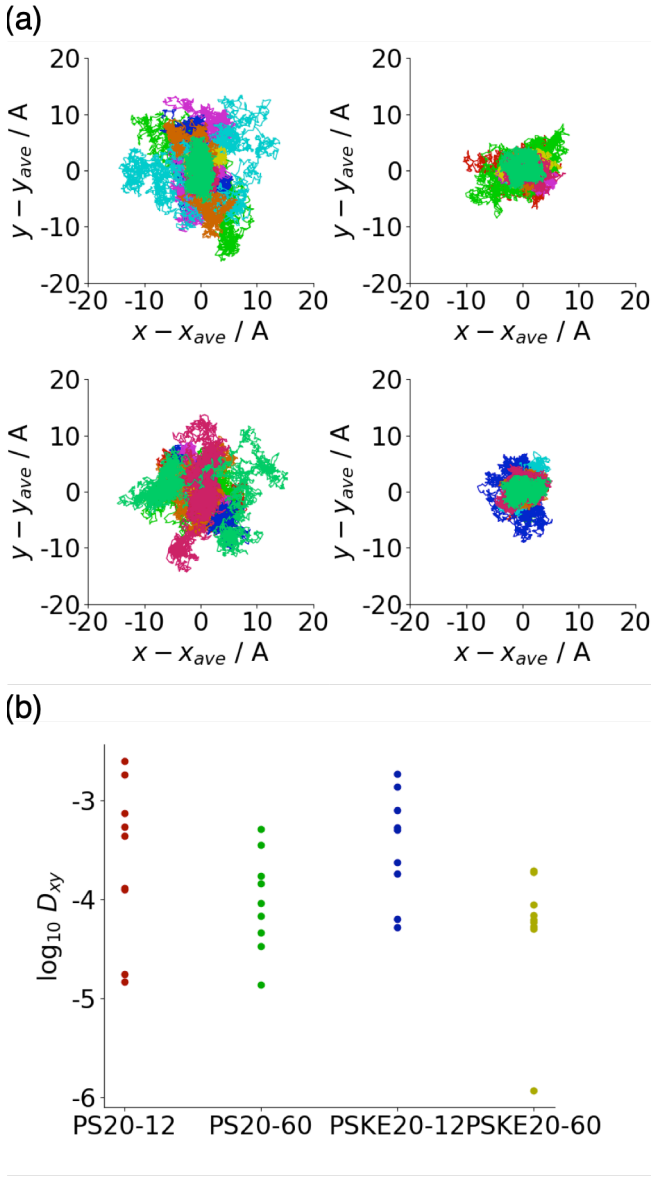

Figure 11: (a)Protein motion in xy-plane over last 50 ns of each simulation for PS20, Nchain=12 (top left), PS20, Nchain=60 (top right), PSKE20, Nchain=12 (bottom left), and PSKE20, Nchain=60 (bottom right). Black, red, green, blue, yellow, purple, turquoise, cyan, and magenta denote runs 1-9 respectively. (b) Lateral diffusion coefficients (in $Å^2$ ps^{-1}) calculated over last 50 ns of each simulation.